Multifunctional Nanopore Electrode Array Method for Characterizing and Manipulating Single Entities in Attoliter-Volume Enclosures

Seol Baek[1], Allison R. Cutri[1], Donghoon Han[2], Seung-Ryong Kwon[3], Julius Reitemeier[1], Vignesh Sundaresan[4#], and Paul W. Bohn[1,4*]

[1]Department of Chemistry and Biochemistry, University of Notre Dame, Notre Dame, Indiana 46556, USA

[2]Department of Chemistry, The Catholic University of Korea, Bucheon, Gyeonggi-do 14662, South Korea

[3]Department of Chemistry and Research Institute of Natural Science, Gyeongsang National University, Jinju, 52828, South Korea

[4]Department of Chemical and Biomolecular Engineering, University of Notre Dame, Notre Dame, Indiana 46556, USA

[*]Author to whom correspondence should be addressed, *pbohn@nd.edu*.

[#]Current address: Department of Chemistry and Biochemistry, University of Mississippi, University, MS 38677.

Abstract

Structurally regular nanopore arrays fabricated to contain independently controllable annular electrodes represent a new kind of architecture capable of electrochemically addressing small collections of matter - down to the single entity (molecule, particle, biological cell) level. Furthermore, these nanopore electrode arrays (NEAs) can also be interrogated optically to achieve single entity spectroelectrochemistry. Larger entities such as nanoparticles and single bacterial cells are investigated by dark-field scattering and potential-controlled single cell luminescence experiments, respectively, while NEA-confined molecules are probed by single molecule luminescence. By carrying out these experiments in arrays of identically constructed nanopores, massively parallel collections of single entities can be investigated simultaneously. The multilayer metal-insulator design of the NEAs enables highly efficient redox cycling experiments with large increases in analytical sensitivity for chemical sensing applications. NEAs may also be augmented with an additional orthogonally designed nanopore layer, such as a structured block copolymer, to achieve hierarchically organized multilayer structures with multiple stimulus-responsive transport control mechanisms. Finally, NEAs constructed with a transparent bottom layer permit optical access to the interior of the nanopore, which can result in cutoff of far-field mode propagation, effectively trapping radiation in an ultrasmall volume inside the nanopore. The bottom metal layer may be used as both working electrode and optical cladding layer, thus producing bifunctional electrochemical zero-mode waveguide architectures capable of carrying out spectroelectrochemical investigations down to the single molecule level.

Introduction

Nanopores are attracting ever-increasing attention both for enabling fundamental advances in measurement science as well as enabling new technologies. Inspired by the ground-breaking fluidic pulse sensing work of Coulter,[1] which opened the door to detecting and enumerating single entities,[2] investigators have pursued applications of small-scale pores to molecular and nanoparticle analysis in addition to exploiting the special properties of fluid flow at the nanometer length scale. Subsequently, the human genome project in the 1990s prompted researchers to turn their attention to DNA sequencing,[3] which naturally highlighted the interaction of macromolecules with both synthetic and natural nanopores[4] and raised the important technological problem of single nucleobase discrimination.[5] Contemporary extensions of these investigations now target the more difficult problem of protein sequencing with single amino acid resolution.[6,7] Similarly, in the 1960s Rice and Whitehead pioneered the first quantitative descriptions of electrokinetic transport in nanocylindrical channels,[8] drawing attention to the importance of the Debye length as a scaling parameter for understanding ionic fluid flow at the nanoscale.[9] Once the special electrokinetic properties of nanochannels were understood, researchers turned to exploiting them to achieve unprecedented fluidic sample manipulations, such as sample stacking for analyte pre-concentration,[10] digital electrokinetic coupling in nanocapillary switches for 3D fluidic integration,[11] and ionic diodes exhibiting ion flow rectification.[12]

At the heart of all of these advances lies a set of unique nanoscale phenomena that are predicated on the relationship of the size of the structure to physical scaling lengths – thus enabling a range of advantages accruing to nanoscale experiments, namely: (*a*) new phenomena; (*b*) surface-to-volume ratio; (*c*) enhanced transport; and (*d*) structures that are commensurate in size with (bio)molecules. For example, electromagnetic radiation accesses novel phenomena in devices smaller than the optical wavelength,[13,14] and electronic transport is sensitive to the ratio of structure size to the carrier scattering length.[15,16] Of particular relevance to the work described here are the screening lengths that apply to

electrified fluids, such as the charge screening, or Debye, length, λ_D.[17] In addition to accessing novel physical interactions on the nanoscale, researchers have exploited the enhanced surface-to-volume ratio in nanochannels to direct ion transport and achieve de-salting of brackish,[18] as well as efficient diffusive delivery of reaction substrates in structures with ultrasmall Peclet numbers, $Pe \ll 1$, to achieve reactions with unit efficiency.[19,20] Finally, nanofabrication capabilities are now sufficiently developed to design and construct artificial nanostructures that are commensurate in size with biological macromolecules and molecular assemblies.[21-23] These structures open possibilities for hybrid artificial-natural assemblies capable of controlling the directionality of reaction processes - similar to the way multi-molecular biomolecular assemblies achieve directional couple cellular processes to vectorial energy sources, such as electromagnetic radiation or proton concentration gradients. Exploiting these vectorial couplings has already resulted in applications in controlled delivery of therapeutic agents,[24,25] catalyzed reaction cascades,[26,27] and high-efficiency light harvesting,[28] to name a few.

In light of these advances, it is natural to ask how nanopores can be combined with redox-capable electrode structures, *i.e.* electrochemical nanopores, to achieve new kinds of electrochemical transformations. For example, Fan and Bard developed architectures in which redox molecules are sequestered in the volume between a conductive substrate and a scanning electrochemical microscopy tip, to achieve ultraefficient redox cycling.[29] Using a similar strategy, Unwin and coworkers acquired current traces with definable single oxidation and reduction event characteristics.[30] These approaches have been successfully applied to nanoparticles,[31] vesicles,[32] and droplets,[33] using nanopipettes housing recessed electrodes, the position of which can be controlled in 3D.

Alternatively, single nanopores can be replaced by arrays of nanopores containing 1, 2, or even 3 internal electrodes,[34,35] to produce structures that exploit hemispherical diffusion profiles and sequester the target entities within the internal volume of the nanopore. Examples of the structural and functional characteristics of such nanopore electrode arrays (NEAs) are shown in **Figure 1**. In this Methods paper,

we highlight four specific experiments that are enabled by the NEA architecture. (1) The nanocylindrical geometry is nearly ideal for the capture and sequestration of single supermolecular entities such as nanoparticles or whole bacterial cells.[36,37] Once captured, the entities may be studied using electrochemistry, spectroscopy, or a combination of the two. (2) The presence of two closely spaced (d ~ 100 nm) electrodes enables high efficiency redox cycling resulting in large increases in analytical sensitivity.[38,39] (3) The planar assembly presenting parallel electrochemical nanopores is ideally suited for the fabrication of hierarchically organized structures, which can provide an additional set of molecular selection and/or transport control properties.[40] (4) Multifunctional structures, in which two or more perturbations can be applied simultaneously, are also possible. For example, the electrochemical zero-mode waveguide (E-ZMW) integrates optical access with a working electrode that doubles as the optical cladding layer of the ZMW.[41-45] The experiments described in this manuscript build upon ideas developed previously in our laboratory. However, the specific examples extend these to new systems and capabilities. They illustrate the distinctive characteristics of NEAs - their ultrasmall volumes which facilitate rapid diffusive transport, the ability to trap optical radiation, and multiple metal-insulator pairings which make multi-electrode experiments possible and demonstrate these capabilities by applying them to systems of molecules, nanoparticles, and single bacterial cells.

Nanoparticle Capture and Characterization

Nanoparticles (NPs) are useful in applications ranging from catalysis to chemical sensing, yet studying their behavior on an individual basis still presents a challenge. In order to measure the properties of individual nanoparticles, capturing and trapping them in a confined space is beneficial, because a one-to-one correspondence can be established between NPs and nanopores, ensuring that only one particle is measured at a time. Furthermore, NEAs make it possible to study massively parallel collections of individual particles simultaneously.

In this section, we explore the capture and optical monitoring of arrays of single NPs in NEAs. Focused ion beam (FIB) milled NEAs with top and bottom diameters of 200 nm and 100 nm, respectively, (thickness = 300 nm) are used to capture 80 nm diameter individual silver nanoparticles. **Figure 2(a)** and **2(b)** show the bright-field and dark-field optical microscope images, respectively, of an 11 × 11 NEA. Since the inner diameter is below the cutoff for propagation of far-field modes at visible wavelengths, the bright-field image does not exhibit normal transmission, as indicated by the array of black regions corresponding to the nanopores. Conversely, the dark-field mode blocks the trans-illumination, but it efficiently captures light scattered by the individual nanopores, which are observed as an array of bright spots, as shown in **Figure 2(b)**.

Introduction of 100 μL of a 7.8 x 10^9 particles mL^{-1} (13 pM) solution of 80 nm diameter Ag NPs to the NEA substrate results in a volume-averaged NP-pore occupancy $\langle n_{pore} \rangle << 1$. However, when an individual NP stochastically enters a nanopore, the scattering intensity emanating from the nanopore increases because of the plasmonic characteristics of the AgNP. **Figure 2(c)** shows a scattering intensity-time trace of a single nanopore, obtained from a movie of intensities of the entire 121 nanopore array, in which the scattering intensity, I_S, undergoes a discontinuous increase, remains stable at a higher level for a few seconds, then returns to the initial intensity. The interpretation of these data is indicated in the schematic diagram shown in the inset. The baseline scattering intensity obtained from 0 s to ~40 s corresponds to an empty nanopore. Then, a NP enters the pore and is trapped by a combination of electrostatic and hydrophobic forces, increasing I_S. Subsequently, the NP departs from the nanopore (~42 s), and I_S returns to the original baseline value, supporting the interpretation that this intensity arises from scattering of the empty nanopore. The increase in scattering intensity can also be seen in the optical images shown in the inset of **Figure 2(c)**. **Figure 2(d)** shows an intensity-time trace of another nanopore where the nanoparticle shows a longer residence time (~20 s) compared to **Figure 2(c)** (~4 s). The NP-to-NP variation in residence time could be due to variations in NP zeta potential, surface charge of the

individual nanopores, or the time-average axial position of the NP within the nanopore. However, it is clear that the scattering intensity is changed quantitatively by the presence of a NP, thereby making it a marker for the capture of NPs by the nanopores.

In comparison to nano-impact electrochemical methods, dark-field optical monitoring of NP capture by NEAs provides several advantages. First, the capture of many individual nanoparticles can be studied simultaneously, enabling high-throughput studies which can quickly determine statistical characteristics of the NP ensemble. Second, the multilayer architecture of NEAs makes it possible to control the chemical environment of the NPs in ways that are not possible with planar electrodes, for example by chemically derivatizing the insulator segments of the repeated metal-insulator, $(MI)^n$, structures. Finally, because NEAs can host multiple electrodes, each electrode can be assigned a separate function. In comparison to our previously published experiments which demonstrated that the outer electrode(s) can serve as an electrical gate, controlling the entry of NPs into the lower portion of the nanopore,[36] the current work illuminates the dynamic character of the capture event by exploiting simple dark-field scattering measurements over time, making it possible to categorize the capture/trapping events into families of characteristic behaviors.

Arrays of Single Bacterial Cells

The ability to capture and detect single molecules has enabled studies of reaction rates, molecular heterogeneity, protein folding, and catalysis.[46-50] More recently research has targeted larger entities, such as single bacterial cells,[51,52] in an effort to understand variations in phenotype at the single cell level and to relate these to public health.[53,54] Examples include the Chemistrode for detection of single cells in a multispecies population,[55] microfluidic confinement of cells in water-in-oil droplets to induce quorum sensing,[56] droplet based microfluidic chips for downstream sequencing,[57] and single-cell motility via flagellar movement with optical tracking.[58] Here we describe a vertical bacterial cell capture/interrogation

motif based on a larger version of the electrochemical-zero mode waveguide (E-ZMW),[59] which we term micropore electrode arrays (MEA). These devices are capable of capturing and trapping single microbial cells, separating them from the bulk, and then interrogating them spectroelectrochemically.

Device design and fabrications strategies adapted from methods to produce E-ZMWS and embedded annular nanoband electrodes (EANEs) developed in this laboratory,[59,60] are described in the **Supporting Information (SI)**. Two parameters can be adjusted to bias the system toward effective capture and trapping of bacterial cells within the micropores: the pore dimensions, and the loading conditions. FIB milling is used to adjust the dimensions of the micropores to match the average dimensions of a single bacterial cell. *Pseudomonas aeruginosa*, the bacterium of choice in these experiments, is *ca.* 0.5-0.8 μm in diameter and 1.5-3.0 μm in length. Thus, pores are designed to a depth of ~ 5.5-6.0 μm, with a width of ~0.7 μm at the working electrode (WE), to accommodate a single cell without admitting a second cell at the imaging plane, which could interfere with spectroelectrochemical measurements. Importantly, the design shown in **Figure 3(a)** captures bacterial cells in a vertical orientation, although other device designs under study in our laboratory bias the capture to a horizontal orientation. Clearly, the micropore geometry can be altered to accommodate bacteria of different sizes and shapes.

In addition, successful capture allows the bacteria to reach the bottom of the micropore, where they can be interrogated electrochemically and spectroscopically imaged. Typically, a 100-μL aliquot of planktonic *P. aeruginosa* culture at OD_{600} = 1.0 is added to a PDMS well attached to the MEA device. The bacteria are then allowed to move freely for *ca.* 3 h – a time sufficient for bacterial capture in the MEA. Interestingly, allowing the cells to move freely into the pores is more effective than capture in the presence of a positive potential. When the device is fully optimized and loaded, the 11 × 11 array allows the study of a large number of single *P. aeruginosa* cells simultaneously.

Once the bacteria-MEA structure is prepared, it is mounted on an inverted epi-illumination microscope and connected to a potentiostat to enable simultaneous optical imaging and collection of

electrochemical data. The gold annulus at the bottom of each MEA micropore serves as the WE, and external platinum and Ag/AgCl wires are used as the counter and quasi-reference electrodes, respectively. 458 nm laser radiation illuminates the substrate from the bottom, and fluorescence is collected back through the objective and imaged onto the active area of an EMCCD camera. **Figure 3(b)** shows a typical optical image obtained from a majority-filled MEA under laser illumination. Comparison of this image to a negative control with no bacteria (not shown) confirms that the bright spots are associated with fluorescence from single cells located within the MEA.

Once cell capture and trapping are confirmed, spectroelectrochemical experiments can be performed simultaneously on all the cells in the array. **Figure 3(c)** demonstrates a typical fluorescence intensity time-trace observed from a single *P. aeruginosa* cell. Generally, single cells exhibit potential-dependent fluorescence behavior that is similar to bulk culture in some respects, but with additional subpopulations showing distinct behaviors. The potential-modulated fluorescence shown in **Figure 3(c)** is one such behavior, which we interpret as arising from surface proximal flavoenzymes in the outer bacterial membrane of Gram-negative *P. aeruginosa*. The isoalloxazine chromophore of flavin adenine dinucleotide (FAD) is known to exhibit potential-dependent emission,[61] consistent with the potential-dependent fluorescence modulation shown in **Figure 3(c)**. A second, less common behavior involves a relatively constant fluorescence emission floor interrupted by large fluorescence emission transients. Finally, a small fraction of the population exhibits no discernible potential dependence, *i.e.*, random emission intensity *vs.* potential. Population statistics, obtained from > 3,000 individual bacterial cells, indicate that *P. aeruginosa* populations exhibit 63% potential-dependent, 29% random, and 8% transient spike behaviors, while a much smaller sample of *E. coli* gives 44%/40%/16%, respectively. Furthermore, the population distribution is strongly dependent on the conditions under which the bacteria are grown as well as other environmental conditions to which the culture may be exposed. For example, the level of nutrition available to the cells has been shown to affect the observed fluorescence behaviors, with

dramatic differences observed between high nutritional states *vs.* starvation. These behaviors, which had previously been obscured in bulk culture studies, present new opportunities to understand single cell phenotype differences and to correlate them with environmental conditions, *e.g.* nutrition level, presence of threats, quorum sensing, *etc.* Thus, the capture of large arrays of single microbial cells opens new avenues for fundamental studies, as well as the development of new technologies based on the detection and spectroelectrochemical behavior of bacterial cell arrays.

Redox Cycling

Turning from relatively large entities such as NPs and microbial cells, we immediately face the challenge that electrochemical experiments suffer from high intrinsic Johnson noise, rendering the detection of a single molecule, or even a few molecules, difficult. An effective strategy to increase the signal-to-noise ratio (SNR) in voltammetric experiments is to incorporate structures that support redox cycling (RC), for example two closely spaced, individually addressable electrodes.[62-66] In RC an initial redox transfer reaction creates a product which then is transported to a nearby electrode where it undergoes the opposite redox reaction, after which it can move back to the original electrode, and so on. In this mechanism the same molecule can be oxidized and reduced many times, thereby amplifying the current signal. To initiate RC, the device is operated in generator-collector (GC) mode, where the potential of one electrode (generator) is swept, while the potential of the other electrode (collector) is held constant at a potential complementary to that yielding the product at the generator.

When implementing RC in 2-electrode NEAs, multiple design parameters can be tuned to maximize cycling efficacy. First, the interelectrode spacing plays a crucial role,[67] and decreasing electrode separation can improve cycling performance. To provide sufficient electrical insulation while maintaining small spatial separation in MIM NEAs, SiN_x insulating layers are commonly placed between the electrodes to produce spacings as low as 60 nm.[68] Next, the transport properties of the system are determined by the

nanopore pitch, thus influencing cycling efficiency. In conventional voltammetry, high-density arrays of recessed electrodes result in substantial overlap of diffusive transport layers, ultimately diminishing mass transport rates due to analyte competition.[69] In contrast, RC experiments benefit from high-density arrays, because redox molecules that escape one nanopore can be recaptured by an adjacent nanopore and continue to contribute to cycling currents. Finally, nanoscale phenomena can be exploited by designing the nanopore diameter to be commensurate with the Debye length, resulting in permselective cation accumulation in negatively charged nanopores.[68,70] In the absence of supporting electrolyte, charged redox analytes experience further enhanced mass transport that arises from ion migration as a result of strong unscreened electric fields between two closely spaced electrodes. The ion accumulation and migration effects interact synergistically to yield currents amplified as much as 2000x.[70] A formal way to characterize the current enhancement in RC experiments is provided by the amplification factor (AF), defined as the ratio of the limiting current in GC mode to that in non-GC mode. AF is strongly dependent on capture efficiency, Φ, defined as the ratio of the limiting current at the collector electrode to that at the generator electrode. High-density nanopore arrays typically exhibit capture efficiencies $\Phi \geq 99\%$.[67,70,71]

Cycling behavior of the reversible $2e^-/2H^+$ reaction between 4-ethylcatechol and 4-ethylquinone, shown in **Figure 4(a)**, is studied here using a ring-disk 2-electrode NEA system, illustrated schematically in **Figure 4(b)**. To initiate redox cycling, the device is operated in GC mode by poising the top electrode at an oxidizing potential while sweeping the potential of the bottom electrode from positive to negative. A solution of 100 μM 4-ethylcatechol in phosphate buffer (pH = 6.8) and 2 M KNO_3 produces the voltammograms shown in **Figure 4(c)**. A clear peak-shaped voltammogram is observed in non-GC mode, **Figure 4(c)** inset, consistent with a transport-limited reaction with substantial diffusional overlap on the high-density array. In contrast, operating the device in GC mode yields two sigmoidal waves, indicating efficient redox cycling with a 21-fold current enhancement.

Multiple benefits arise from detecting electroactive species using redox cycling, the most apparent

being the increased SNR and sensitivity resulting from RC operation.[64,66] RC can also significantly improve selectivity. While conventional electrochemical detection is only moderately selective, RC operation restricts electrochemical transformations to reversible redox species, with irreversible species being depleted after the initial redox reaction, providing one avenue to achieve selectivity. Furthermore, RC can result in charge state flipping (cation/neutral or neutral/anion) which, combined with the permselective properties of nanopores, can lead to enormous enhancements in selectivity. Previously, we demonstrated this in our laboratory in the dopamine/ascorbic acid system at ultralow ionic strength (absence of supporting electrolyte) to obtain selectivity ratios as high as 3000x.[72] Another strategy to differentiate between two reversible redox species with similar redox potentials, poises the applied potentials to force a response of both species at the generator electrode while the collector electrode potential is chosen so that only one product of the pair reacts.[73,74] Here, these capabilities are extended from the simple model systems shown previously to NEA-mediated redox cycling for the determinations of environmentally relevant diols.

Hierarchically Organized Gatable Structures

The functionality of NEAs can be extended through hierarchically organized structures, prepared by adding layers to the NEA surface, thereby endowing the composite structure with additional transport selectivity. Previously, we had demonstrated transport control through the addition of relatively impermeable poly(dimethylsiloxane) and cation permselective Nafion.[75,76] Here, we extend our recent application of the use of smart membranes in which transport is controllable both by pH and by applied potential across the membrane. Block copolymer (BCP) membranes offer one attractive way to accomplish this. BCPs self-assemble by microphase separation into highly-ordered, high-density nanostructures with various shapes and dimensions.[77] For example, densely-packed nanocylindrical assemblies formed in thin BCP films can mimic biological ion-channels for applications such as

biosensors and chemical separations.[78,79] In addition, stimulus-responsive BCPs can be realized by tailoring functional groups in the proper BCP nanodomains.[80] These are useful in regulating ionic/molecular transport in response to external stimuli, *e.g.*, pH, ionic charge, and applied potential.[40] In a hierarchically organized BCP membrane-coated NEA, *i.e.*, BCP@NEA, illustrated schematically in **Figure 5(a)**, ions/molecules selectively-transported through the BCP membrane are captured in the attoliter-volume of the NEA nanopore where they can be detected electrochemically by exploiting the closely-spaced dual electrode configuration for RC. **Figure 5(b)** shows a cross-sectional SEM image of a poly(styrene)-*b*-poly(4-vinylpyridine) (PS-*b*-P4VP) BCP@NEA structure, illustrating the structural integrity of the BCP attached to the NEA surface.

The P4VP cylindrical nanodomains present reversible protonation sites at the pyridine N atoms, yielding pH-dependent transport properties in the vertically aligned nanochannels.[81-84] The nanochannels switch between a swollen, hydrophilic, transport-on state at pH < pKa (~4.8 in PS-*b*-P4VP) and a collapsed, hydrophobic, transport-off state at pH > pKa.[83] When pH < pKa, the swollen, positively charged structure supports anion-permselective transport of aqueous solution across the BCP membrane.[85] However, at higher pH values, water condensation/evaporation dynamics dominate the transport characteristics,[86,87] and ion/water transport is blocked. Thus, pH-responsive gating behavior is obtained in hierarchically organized BCP@NEA structures by designing the pores to be size-commensurate with λ_D (*vide supra*).[88] Interestingly, the magnitude of charge screening and ion rectification decrease with increasing ionic strength in contrast to other transport-control membrane structures, such as Nafion@NEA,[76] due to the larger sizes of the PS-*b*-P4VP nanochannels (diameter ~12 nm), thus establishing experimental control over the extent of permselectivity.

Coupling charge-selective BCP membranes to NEAs is a viable approach to designing sensitive sensors, however, the hydrophobic character of the BCP at pH > pK_a (P4VP) also holds great promise for devising controllable ion channels. At pH > p*K*a (P4VP), the P4VP blocks of the BCP are hydrophobic

and form a dewetted state, *i.e.*, vapor barrier, which blocks the transport of water and consequently ion/molecular permeation, but this state is susceptible to electrowetting by the application of a simple trans-membrane potential. To test this hypothesis, a thin layer of BCP membrane is prepared on a planar Au electrode. Cyclic-voltammetry is then performed on the BCP membrane-coated Au electrode with 2 mM $Fe(CN)_6^{3-}$ in DI water. As shown in **Figure 6**, the voltammetric current response depends on pH, increasing with increasing scan number at $E_{appl} \leq -0.4$ V, implying gradually increased wetting of the hydrophobic BCP nanochannels at more negative potentials. However, when the same BCP membrane is exposed to pH 3.1 aqueous electrolyte, the reversible voltammetric behavior of the $Fe(CN)_6^{3-}$ probe is recovered. Remarkably the pH of the contacting solution completely switches the dominant electrochemical response by controlling access of the redox probe species to the interior of the NEA nanopores through the initially dewetted P4VP nanopores. Thus, the voltammetric behavior at pH > pK_a (P4VP) is determined both by pH and E_{appl}, confirming the potential-controlled gating response of the BCP nanochannels and supporting the central role of wetting/dewetting transitions. Furthermore, because the potential-induced wetting/dewetting transitions are reversible, they can be combined with NEAs to effect capture and trapping of solution into the NEA, where redox species can be measured at high sensitivity with RC.[89] External stimulus-induced wetting/dewetting transitions are likely to find applications in areas such as water separation/purification, controlled-drug release system, and ultrasensitive sensors.

Electrochemical Zero-Mode Waveguides

Zero-mode waveguides (ZMWs) are near-field nanophotonic structures typically fabricated as 50-300 nm diameter cylindrical apertures in a metal film on fused silica via FIB milling. Radiation with wavelength longer than a critical threshold value, $\lambda_c \sim 1.7d$, where d is the pore diameter, is cutoff from far-field propagation, resulting in a ZMW observation volume which is only a fraction of the geometric

volume of the nanopore. Radiation incident on the ZMW from the silica thus couples to an evanescent field with an exponentially decaying amplitude along the axis of the nanopore, and the effective observation zone is limited to a few 10s of nanometers from the silica-metal interface, depending on its diameter. Although Al is widely used for ZMW construction, Au has a number of attractive properties for ZMW applications, such as its resistance to oxidation, a broad range of self-assembly chemistries[90-92] to confer functionality, and its chemical orthogonality to silica, making it possible to direct surface attachment to either Au or silica interior surfaces of the ZMW. Encouraged by these appealing properties, we have elaborated the basic ZMW architecture to produce bifunctional electrochemical-ZMW (E-ZMW) structures, in which the optical cladding layer serves both to confine the radiation and to function as a working electrode to carry out faradaic electrochemistry.[93-95] Furthermore, the chemical orthogonality of Au and SiO_2 means that molecules of interest, such as enzymes, may be directed and immobilized either to the base of the ZMW[96] or to the electrochemically active sidewalls.[93]

The E-ZMW is clearly consilient with the NEA architecture, so we have examined using additional electrodes outside the ZMW optical zone to control the redox environment of the nanopore. For example, single reactive oxygen species (ROS) can be generated *in situ* through the $1e^-$ reduction of O_2 to superoxide and its subsequent disproportionation to yield H_2O_2. This can then be used as a high precision strategy to control the oxidation state of the nanopore volume, which is controlled by the amount of charge injected. For example, glutathione (GSH) and oxidized glutathione dimer (GSSG) can be used as soluble factors, with the enzyme glutathione reductase (GR) immobilized on the bottom ring electrode (optical cladding layer) of the E-ZMW.[43] GR is a flavoenzyme, in which $FADH_2$ prosthetic groups contain an electrofluorogenic isoalloxazine moiety, which exhibits a highly fluorescent oxidized state and a dark reduced state, thus enabling fluorescence trajectories to probe both single electron transfer events and the dispersion in activity among different copies of the same enzyme.

At the beginning of the experiment, the top ring electrode produces H_2O_2, which results in an

increase of the [GSSG]/[GSH] ratio. The bottom electrode is held negative of the GR-FAD equilibrium, so both flavins are present as $FADH_2$ and, thus, only weakly fluorescent at equilibrium. This is consistent with the observation of only a small number of transient emission peaks exceeding the average by > 3σ, where σ is the standard deviation of the fluorescence data. Changing the solution environment to more oxidizing conditions increases [GSSG], which is the substrate of GR. Reduction of GSSG to GSH produces a transient oxidized FAD, which is then quickly converted back to the reduced $FADH_2$, resulting in a fluorescence transient. The detailed time records, therefore, reflect the fluorescence dynamics of GR in the presence of oxidized GSSG, the concentration of which is controlled by H_2O_2 produced at the generator electrode, **Figure 7**. Whereas previously, we had demonstrated to ability to pin the redox state of single immobilized enzymes,[43] this system supports the exploration of a multidimensional phase space for enzyme catalysis with electrochemical control over production of the substrate and single molecule spectroscopy to read out the enzyme dynamics.

Another characteristic of the sub-wavelength pore diameters exhibited by NEA-based E-ZMWs is the zeptoliter scale observation volumes, which can be exploited for high sensitivity observation of freely diffusing species at the single molecule level.[97] The extremely small optical volumes allow single molecule spectroscopic investigations for solution species in the micromolar concentration range. This brings many enzymatic reactions, which exhibit μM-range K_D values, into view.[98] Furthermore, because the potentials of all of the nanopore electrodes can be controlled independently E-ZMWs exhibit bifunctional photonic and electrochemical characteristics. Therefore, E-ZMWs offer an efficient route to monitor real-time single enzyme molecule dynamics *via* simultaneous spectroscopic and electrochemical measurements while enabling simultaneous data acquisition from all of the nanopores in an array.

Following on the studies of immobilized GR homodimer described above, the fluorescence dynamics of freely-diffusing GR molecules are explored at single molecule occupancy under potential control in E-ZMWs.[45] However, free diffusion means that GR molecules only approach the electrode surface

sporadically. In addition, the long electron transfer distance between the electrode surface and the $FADH_2$/FAD active sites, make direct electron transfer inefficient and result in potential-independent GR fluorescence in response to direct electron transfer. Therefore, methyl viologen (MV^{2+}) is used as a redox mediator for FAD (GR) reduction, and MV/GR-containing nanopores respond to applied potential according to the reaction scheme shown in **Figure 8(a)**. Under conditions where the time-averaged occupancy of a single pore is $\langle n_{pore} \rangle$ ~ 0.8, weak fluorescence is obtained from the array at potentials more negative than E_{eq} for $MV^{2+/+\bullet}$ (E_{appl} = –0.95 V *vs*. Ag/AgCl), and much stronger fluorescence at oxidizing potentials (E_{appl} = –0.75 V *vs*. Ag/AgCl), as shown in **Figure 8(b)**. Finally, **Figure 8(c)** shows that even at the level of a single pore there is a significant difference in fluorescence intensities caused by the efficient MV-mediated cycling of GR between reduced ($FADH_2$) and oxidized (FAD) states. Control experiments (not shown) also demonstrate that the fluorescence behavior requires the presence of all three species: mediator MV^{2+}, enzyme GR, and substrate GSSG, in a concentration-dependent manner. Thus, the zeptoliter-volume environment achieved in E-ZMWs enables investigations of potential-dependent single enzyme molecule behavior under conditions where the redox environment can be tightly controlled.

IV. Conclusions

The NEA construct described in this paper constitutes a versatile platform for the investigation of small collections of matter, down to the level of a single entity. Precise control over NEA geometry makes it possible to carry out electrochemical manipulations under highly controlled conditions, and the ability to incorporate 1, 2, or 3 annular electrodes gives rise to a large array of different redox control paradigms. In addition to the canonical cyclic voltammetry and differential pulse voltammetry carried out at a single working electrode, simultaneous control of the potential at two closely spaced electrodes makes it possible to carry out more sophisticated experiments involving redox cycling and *in situ* reagent generation. Furthermore, the NEAs may be constructed with a transparent bottom layer, giving optical

access to the interior of the nanopore. By careful selection of the nanopore geometry and solvent, conditions may be achieved where far-field mode propagation is cutoff, and radiation is effectively trapped in an ultrasmall volume just above the silica base layer. Then, using the bottom metal layer as both working electrode and optical cladding layer produces bifunctional E-ZMW architecture capable of spectroelectrochemical investigations at the single molecule level. Under different design rules, NEA structures maybe prepared that can access larger entities, such as single nanoparticles and bacterial cells. Finally, the NEAs may be augmented with an additional layer, such as a structured nanocylindrical block copolymer, to achieve hierarchically organized multilayer structures capable of sophisticated, stimulus-responsive transport control. These observations collectively establish nanopore electrode arrays as a powerful tool for the study of small collections of matter.

Supporting Information

Supporting Information is available online at the link below. The Supporting Information file contains details of the fabrication of the structures described, including High Precision NEAs, Micropore Electrode Arrays, Massively Parallel Arrays, Post-fabrication Processing, and Block Copolymer Membrane-Coated NEAs, as well as figures showing the structures in various phases of fabrication.

Acknowledgements

Work described here was supported by grants from the National Science Foundation (CHE 1904196), the National Institute of Allergies and Infectious Diseases (1R21GM126246-06), and the Department of Energy Office of Basic Energy Sciences (DE FG02 ER15851). The authors also gratefully acknowledge the Notre Dame Nanofabrication Facility and the Notre Dame Integrated Imaging Facility, for their expert assistance in device fabrication and characterization.

References

[1] W. H. Coulter, (U.S. Patent 2,656,508 A, U.S. Patent 2,656,508 A, Oct 20, 1953).

[2] R. W. DeBlois and C. P. Bean, Rev. Sci. Instrum. **41,** 909 (1970).

[3] H. Swerdlow, J. Z. Zhang, D. Y. Chen, H. R. Harke, R. Grey, S. L. Wu, N. J. Dovichi, and C. Fuller, Analyt. Chem. **63,** 2835 (1991).

[4] D. Branton, D. W. Deamer, A. Marziali, H. Bayley, S. A. Benner, T. Butler, M. Di Ventra, S. Garaj, A. Hibbs, X. H. Huang, S. B. Jovanovich, P. S. Krstic, S. Lindsay, X. S. S. Ling, C. H. Mastrangelo, A. Meller, J. S. Oliver, Y. V. Pershin, J. M. Ramsey, R. Riehn, G. V. Soni, V. Tabard-Cossa, M. Wanunu, M. Wiggin, and J. A. Schloss, Nat. Biotechnol. **26,** 1146 (2008).

[5] S. Howorka, S. Cheley, and H. Bayley, Nat. Biotechnol. **19,** 636 (2001).

[6] Z. L. Hu, M. Z. Huo, Y. L. Ying, and Y. T. Long, Angew. Chem. Int. Ed. **60,** 14738 (2021).

[7] J. Wilson, L. Sloman, Z. R. He, and A. Aksimentiev, Adv. Funct. Mater. **26,** 4830 (2016).

[8] C. L. Rice and R. Whitehead, J. Phys. Chem. **69,** 4017 (1965).

[9] C. Ho, R. Qiao, J. B. Heng, A. Chatterjee, R. J. Timp, N. R. Aluru, and G. Timp, Proc. Natl. Acad. Sci. USA **102,** 10445 (2005).

[10] J. Khandurina, S. C. Jacobson, L. C. Waters, R. S. Foote, and J. M. Ramsey, Analyt. Chem. **71,** 1815 (1999).

[11] T.-C. Kuo, L. A. Sloan, J. V. Sweedler, and P. W. Bohn, Langmuir **17,** 6298 (2001).

[12] R. Karnik, C. Duan, K. Castelino, H. Daiguji, and A. Majumdar, Nano Lett. **7,** 547 (2007).

[13] W. L. Barnes, A. Dereux, and T. W. Ebbesen, Nature **424,** 824 (2003).

[14] K. A. Willets and R. P. Van Duyne, Annu. Rev. Phys. Chem. **58,** 267 (2007).

[15] T.-W. Hwang, S. P. Branagan, and P. W. Bohn, J. Am. Chem. Soc. **135,** 4522 (2013).

[16] Y. Zhang, R. H. Terrill, T. A. Tanzer, and P. W. Bohn, J. Am. Chem. Soc. **120,** 9969 (1998).

[17] P. W. Bohn, Ann. Rev. Analyt. Chem. **2,** 279 (2009).

[18] K. N. Knust, D. Hlushkou, U. Tallarek, and R. M. Crooks, Chemelectrochem **1,** 850 (2014).

[19] I. Gibson, L.R., S. P. Branagan, and P. W. Bohn, Small **9,** 90 (2013).

[20] V. V. Swaminathan, I. Gibson, L.R., M. Pinti, S. Prakash, P. W. Bohn, and M. A. Shannon, J. Nanopart. Res. **14,** 951 (2012).

[21] Y. Ahmadi, E. De Llano, and I. Barisic, Nanoscale **10,** 7494 (2018).

[22] X. Ji, C. Xiao, W.-F. Lau, J. Li, and J. Fu, Biosens. Bioelectron. **82,** 240 (2016).

[23] G. M. L. Messina, C. Passiu, A. Rossi, and G. Marletta, Nanoscale **8,** 16511 (2016).

[24] L. Franceschini, M. Soskine, A. Biesemans, and G. Maglia, Nat. Commun. **4** (2013).

[25] T. S. Metzger, R. Tel-Vered, and I. Willner, Small **12,** 1605 (2016).

[26] K. Peng, H. Zhao, Y. Yuan, R. Yuan, and X. Wu, Biosens. Bioelectron. **55,** 366 (2014).

[27] M. Riedel, W. J. Parak, A. Ruff, W. Schuhmann, and F. Lisdat, ACS Catal. **8,** 5212 (2018).

[28] L. Chen, Y. Honsho, S. Seki, and D. L. Jiang, J. Am. Chem. Soc. **132,** 6742 (2010).

[29] F. R. F. Fan and A. J. Bard, Science **267,** 871 (1995).

[30] J. C. Byers, B. Paulose Nadappuram, D. Perry, K. McKelvey, A. W. Colburn, and P. R. Unwin, Analyt. Chem. **87,** 10450 (2015).

[31] R. J. Yu, Y. L. Ying, R. Gao, and Y. T. Long, Angew. Chem. Int. Ed. **58,** 3706 (2019).

[32] Y. Liu, C. Xu, P. Yu, X. W. Chen, J. H. Wang, and L. Q. Mao, Chemelectrochem **5,** 2954 (2018).

[33] F. O. Laforge, J. Carpino, S. A. Rotenberg, and M. V. Mirkin, Proc. Natl. Acad. Sci. USA **104,** 11895 (2007).

[34] K. Fu, D. Han, C. Ma, and P. W. Bohn, Faraday Disc. **193,** 51 (2016).

[35] S.-R. Kwon, S. Baek, K. Fu, and P. W. Bohn, Small **20,** 1907249 (2020).

[36] K. Fu, D. Han, G. M. Crouch, S.-R. Kwon, and P. W. Bohn, Small **14,** 1703248(1 (2018).

[37] J.-Y. Kim, D. Han, G. M. Crouch, S.-R. Kwon, and P. W. Bohn, Analyt. Chem. **91,** 4568 (2019).

[38] K. Fu, D. Han, C. Ma, and P. W. Bohn, Nanoscale **9,** 5164 (2017).

[39] C. Ma, N. M. Contento, and P. W. Bohn, J. Am. Chem. Soc. **136,** 7225 (2014).

[40] S. Baek, S.-R. Kwon, K. Fu, and P. W. Bohn, ACS Appl. Mater. Interf. **12,** 55116 (2020).

[41] L. P. I. Zaino, D. A. Grismer, D. Han, G. M. Crouch, and P. W. Bohn, Faraday Disc. **184,** 101 (2015).

[42] D. Han, G. M. Crouch, K. Fu, L. P. Zaino, and P. W. Bohn, Chem. Sci. **8,** 5345 (2017).

[43] D. Han, S.-R. Kwon, K. Fu, G. M. Crouch, and P. W. Bohn, in *Electrochemical Zero-Mode Waveguide Studies of Single Enzyme Reactions*, Cork, Ireland, 2019 (IEEE).

[44] V. Sundaresan and P. W. Bohn, Chem. Sci. **11,** 10951 (2020).

[45] S. Baek, D. Han, S. R. Kwon, V. Sundaresan, and P. W. Bohn, Analyt. Chem. **94,** online (2021).

[46] L. A. Baker, J. Am. Chem. Soc. **140,** 15549 (2018).

[47] B. Schuler and H. Hofmann, Curr. Opin. Struct. Biol. **23,** 36 (2013).

[48] H. Ren and M. A. Edwards, Current Opinion in Electrochemistry **25,** 100632 (2021).

[49] H.-W. Wang, S.-M. Lu, M. Chen, and Y.-T. Long, Current Opinion in Electrochemistry**,** 100999 (2022).

[50] K. Fu, S.-R. Kwon, D. Han, and P. W. Bohn, Accounts of Chemical Research**,** acs.accounts.9b00543 (2020).

[51] D. D. Doorneweerd, W. A. Henne, R. G. Reifenberger, and P. S. Low, Langmuir **26,** 15424 (2010).

[52] S. Pahlow, S. Stöckel, S. Pollok, D. Cialla-May, P. Rösch, K. Weber, and J. Popp, Analyt. Chem. **88,** 1570 (2016).

[53] A. Talebi Bezmin Abadi, A. A. Rizvanov, T. Haertlé, and N. L. Blatt, BioNanoScience **9,** 778 (2019).

[54] C. A. Michael, D. Dominey-Howes, and M. Labbate, Frontiers in Public Health **2** (2014).

[55] W. Liu, H. J. Kim, E. M. Lucchetta, W. Du, and R. F. Ismagilov, Lab Chip **9,** 2153 (2009).

[56] J. Q. Boedicker, M. E. Vincent, and R. F. Ismagilov, Angew. Chem. Int. Ed. **48,** 5908 (2009).

[57] K. Leung, H. Zahn, T. Leaver, K. M. Konwar, N. W. Hanson, A. P. Page, C. C. Lo, P. S. Chain, S. J. Hallam, and C. L. Hansen, Proc. Natl. Acad. Sci. USA **109,** 7665 (2012).

[58] K. Zhao, B. S. Tseng, B. Beckerman, F. Jin, M. L. Gibiansky, J. J. Harrison, E. Luijten, M. R. Parsek, and G. C. L. Wong, Nature **497,** 388 (2013).

[59] J. Zhao, L. P. Zaino Iii, and P. W. Bohn, Faraday Disc. **164,** 57 (2013).

[60] S. P. Branagan, N. M. Contento, and P. W. Bohn, J. Am. Chem. Soc. **134,** 8617 (2012).

[61] Y.-T. Kao, C. Saxena, T.-F. He, L. Guo, L. Wang, A. Sancar, and D. Zhong, Journal of the American Chemical Society **130,** 13132 (2008).

[62] A. J. Bard, J. A. Crayston, G. P. Kittlesen, T. Varco Shea, and M. S. Wrighton, Analyt. Chem. **58,** 2321 (1986).

[63] J. E. Bartelt, M. R. Deakin, C. Amatore, and R. M. Wightman, Analyt. Chem. **60,** 2167 (1988).

[64] O. Niwa, M. Morita, and H. Tabei, Analyt. Chem. **62,** 447 (1990).

[65] Z. P. Aguilar, W. R. Vandaveer, and I. Fritsch, Analyt. Chem. **74,** 3321 (2002).

[66] B. Wolfrum, M. Zevenbergen, and S. Lemay, Analyt. Chem. **80,** 972 (2008).

[67] C. Ma, N. M. Contento, L. R. Gibson, and P. W. Bohn, ACS Nano **7,** 5483 (2013).

[68] K. Fu, D. Han, C. Ma, and P. W. Bohn, Nanoscale **9,** 5164 (2017).

[69] N. Godino, X. Borrisé, F. X. Muñoz, F. J. del Campo, and R. G. Compton, J. Phys. Chem. C **113,** 11119 (2009).

[70] C. Ma, N. M. Contento, and P. W. Bohn, J. Am. Chem. Soc. **136,** 7225 (2014).

[71] K. Fu, D. Han, C. Ma, and P. W. Bohn, Faraday Discuss. **193,** 51 (2016).

[72] C. Ma, N. M. Contento, L. R. Gibson, and P. W. Bohn, Analyt. Chem. **85,** 9882 (2013).

[73] V. Dam, W. Olthuis, and A. van den Berg, Analyst **132,** 365 (2007).

[74] F. Zhu, J. Yan, M. Lu, Y. Zhou, Y. Yang, and B. Mao, Electrochim. Acta **56,** 8101 (2011).

[75] S.-R. Kwon, K. Fu, D. Han, and P. W. Bohn, ACS Nano **12,** 12923 (2018).

[76] K. Fu, D. Han, S.-R. Kwon, and P. W. Bohn, ACS Nano **12,** 9177 (2018).

[77] H. Feng, X. Lu, W. Wang, N.-G. Kang, and J. W. Mays, Polym. Polym. Compos. **9,** 494 (2017).

[78] L. Guo, Y. Wang, and M. Steinhart, Chem. Soc. Rev. **50,** 6333 (2021).

[79] T. Guo, J. Gao, X. Qin, X. Zhang, and H. Xue, Polym. Polym. Compos. **10,** 723 (2018).

[80] C. Pinto-Gómez, F. Pérez-Murano, J. Bausells, L. G. Villanueva, and M. Fernández-Regúlez, Polymers (Basel) **12,** 2432 (2020).

[81] J. Lindqvist, D. Nyströ̈m, E. Ostmark, P. Antoni, A. Carlmark, M. Johansson, A. Hult, and E. Malmströ̈m, Biomacromolecules **9,** 2139 (2008).

[82] B. Yameen, M. Ali, R. Neumann, W. Ensinger, W. Knoll, and O. Azzaroni, Nano Lett. **9,** 2788 (2009).

[83] Z. Zhang, X.-Y. Kong, K. Xiao, Q. Liu, G. Xie, P. Li, J. Ma, Y. Tian, L. Wen, and L. Jiang, J. Am. Chem. Soc. **137,** 14765 (2015).

[84] Z. Liu, W. Wang, R. Xie, X.-J. Ju, and L.-Y. Chu, Chem. Soc. Rev. **45,** 460 (2016).

[85] Y. Wu, K. Wang, H. Tan, J. Xu, and J. Zhu, Langmuir **33,** 9889 (2017).

[86] M. R. Powell, L. Cleary, M. Davenport, K. J. Shea, and Z. S. Siwy, Nat. Nanotechn. **6,** 798 (2011).

[87] S. N. Smirnov, I. V. Vlassiouk, and N. V. Lavrik, ACS Nano **5,** 7453 (2011).

[88] S. Baek, S.-R. Kwon, K. Fu, and P. W. Bohn, ACS Applied Materials & Interfaces **12,** 55116 (2020).

[89] S.-R. Kwon, S. Baek, and P. W. Bohn, Faraday Disc. **233,** 283 (2022).

[90] D. G. Castner and B. D. Ratner, Surf. Sci. **500,** 28 (2002).

[91] H. Cölfen and S. Mann, Angew. Chem. Int. Ed. **42,** 2350 (2003).

[92] A. Doron, E. Katz, and I. Willner, Langmuir **11,** 1313 (1995).

[93] J. Zhao, L. P. Zaino, and P. W. Bohn, Faraday Disc. **164,** 57 (2013).

[94] D. Han, G. M. Crouch, K. Fu, L. P. Zaino III, and P. W. Bohn, Chem. Sci. **8,** 5345 (2017).

[95] L. P. Zaino, D. A. Grismer, D. Han, G. M. Crouch, and P. W. Bohn, Faraday Discuss. **184,** 101 (2015).

[96] J. Zhao, S. P. Branagan, and P. W. Bohn, Appl. Spectrosc. **66,** 163 (2012).

[97] J. M. Moran-Mirabal and H. G. Craighead, Methods **46,** 11 (2008).

[98] P. Turunen, A. E. Rowan, and K. Blank, FEBS Lett. **588,** 3553 (2014).

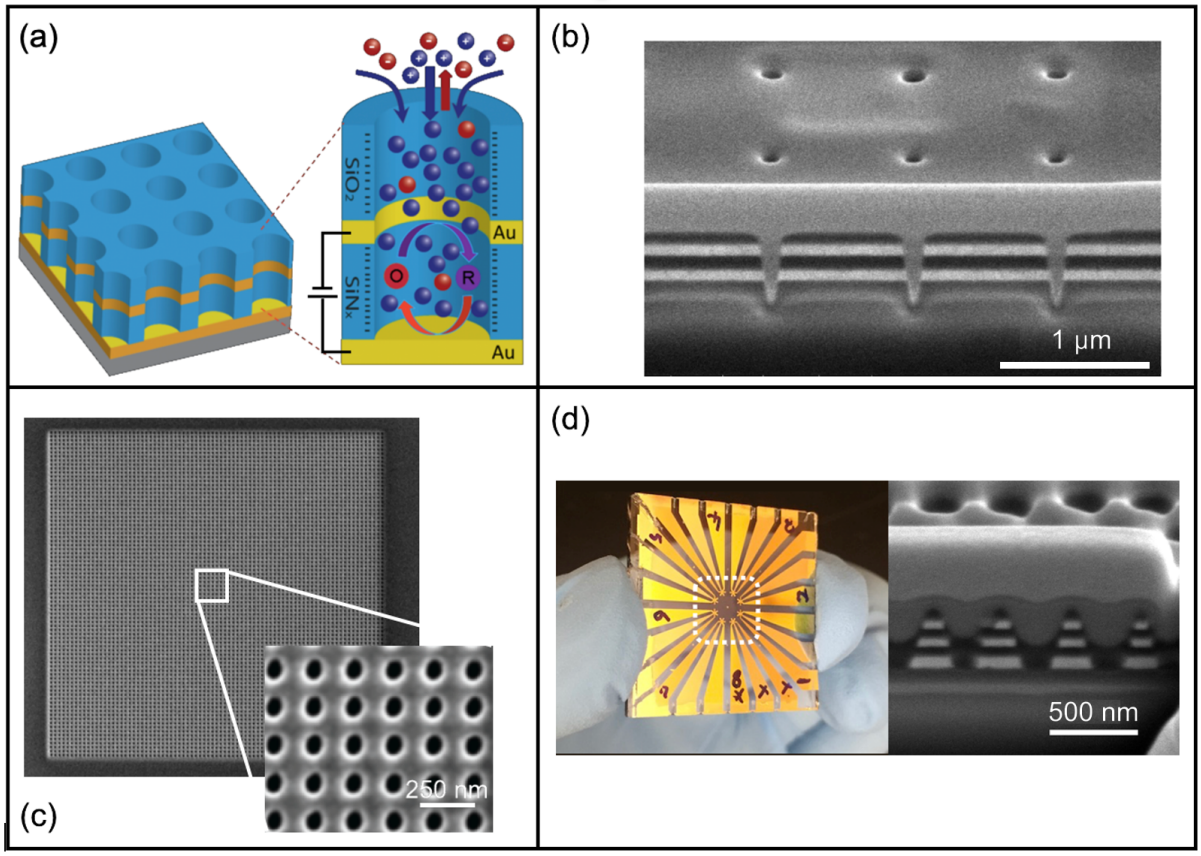

Figure 1. Nanopore electrode arrays. (a) Schematic diagram of a ring-disk 2-electrode NEA. (*Left*) Schematic top cutaway view of a small portion of an array. (*Right*) Operation of a single nanopore from the array. Permselectivity is represented by the excess of cations (blue) inside the nanopore. Redox cycling is indicated by consecutive oxidation at the bottom disk electrode (anode) and reduction at the middle ring electrode (cathode) - converting R to O and back to R. (b) Tilted (52°) cross-sectional SEM image of three side-by-side nanopores from a ring-ring 2-electrode NEA. Lighter areas are Au electrodes. (c) Plan view SEM image of an 81 × 81 NEA. (*Inset*. Magnified image showing the 250 nm pitch and ~100 nm nanopore diameter). (d) (*Left*) Photograph and (*Right*) Tilted (52°) cross-sectional SEM image of four side-by-side nanopores from a ring-ring-ring 3-electrode NEA. Lighter areas are Au electrodes. Note that the bottom Au layer shown in panel (a) can be left intact to serve as a disk electrode, or it can be removed by FIB milling or RIE, as shown in panels (b) and (d), to provide optical access while still functioning as a ring electrode.

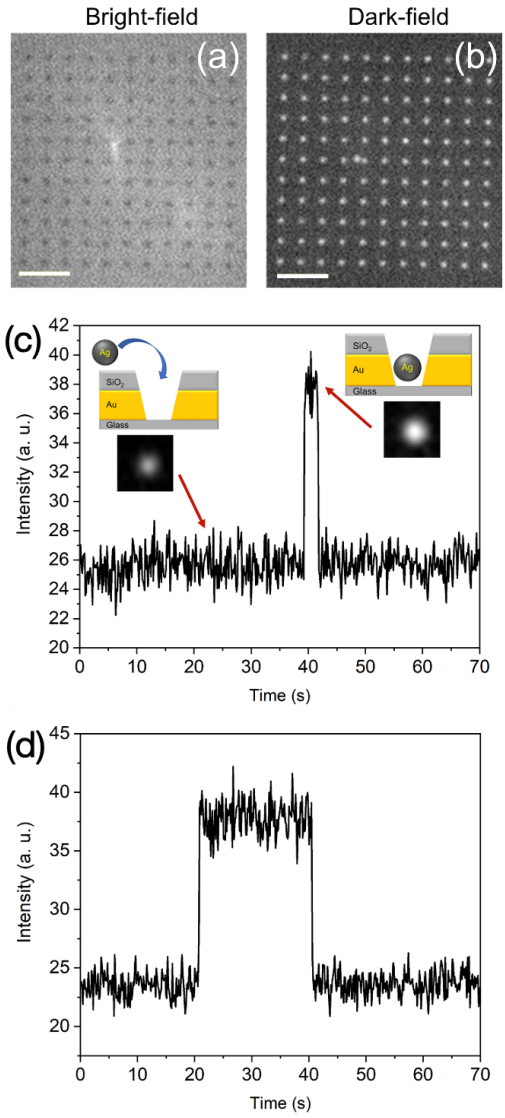

Figure 2. Trans-illumination single nanoparticle imaging in a nanopore electrode array. (a) Bright-field and (b) dark-field optical images of NEAs. Scale bar = 5 μm. (c) and (d) Dark-field intensity time traces of two different nanopores, showing different characteristic behaviors. (c, *inset*) Dark-field optical images of nanopore before and after the insertion of Ag NP and schematic illustrations for both cases.

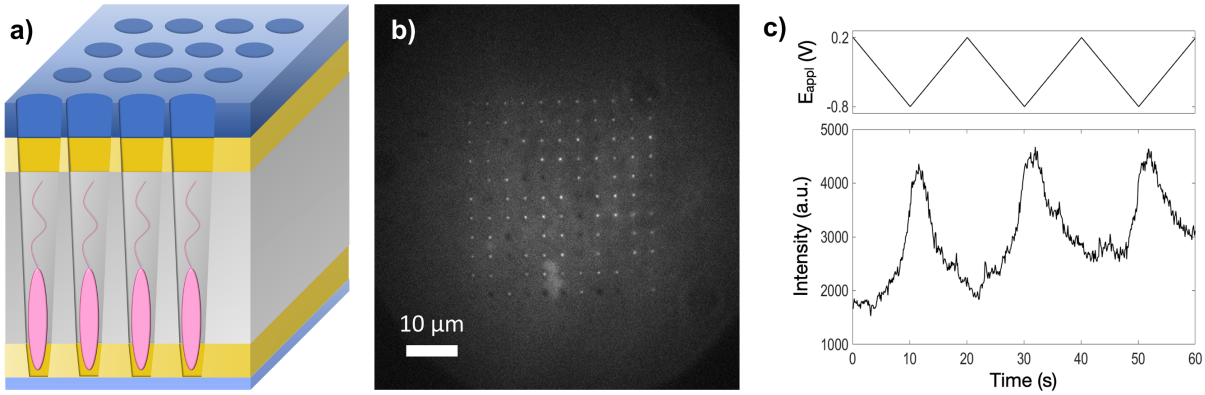

Figure 3. Micropore electrode array (MEA) spectroelectrochemistry of single bacteria cells. (a) Schematic illustration depicting a cross-section of the MEA with trapped bacteria. From bottom to top, the device is made of Au/SU-8/Au/SiO_2 layered using sequential deposition. Although the bacteria are depicted residing at the bottom Au layer, which serves as the working electrode, their actual position can be anywhere along the micropore. (b) A 100 ms frame taken from a fluorescence microscopy movie. Bright spots are associated with fluorescence from flavoenzymes in single cells located within the MEA. (c) An intensity time-trace of a single pore in the MEA. This bacterial cell demonstrates fluorescence that is modulated as E_{appl} *vs.* Ag/AgCl is swept between oxidizing and reducing potentials.

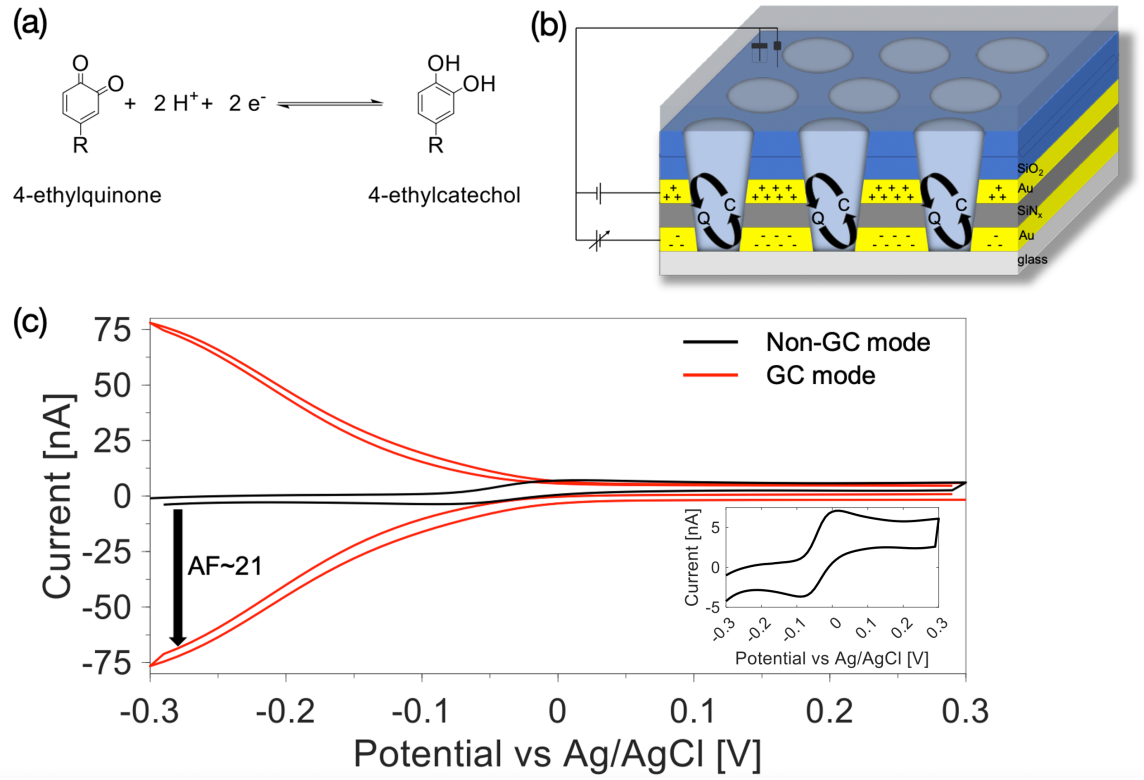

Figure 4. High efficiency redox cycling in NEAs. (a) Reversible $2e^-/2H^+$ reaction of 4-ethylcatechol and 4-ethylquinone. (b) Schematic illustration representing redox cycling in the 2-electrode NEA device in GC mode. C and Q denote 4-ethylcatechol and 4-ethylquinone, respectively. (c) Voltammograms of 100 μM 4-ethylcatechol in 2 M KNO_3 phosphate buffer (pH = 6.8) operated in non-GC (black and inset) and GC (red) modes. The inset enlarges the voltammogram in non-GC mode 25-fold. In GC mode, the top electrode is poised at +0.3 V vs Ag/AgCl while the potential of the bottom electrode is swept over the indicated range at a scan rate of 100 mV/s.

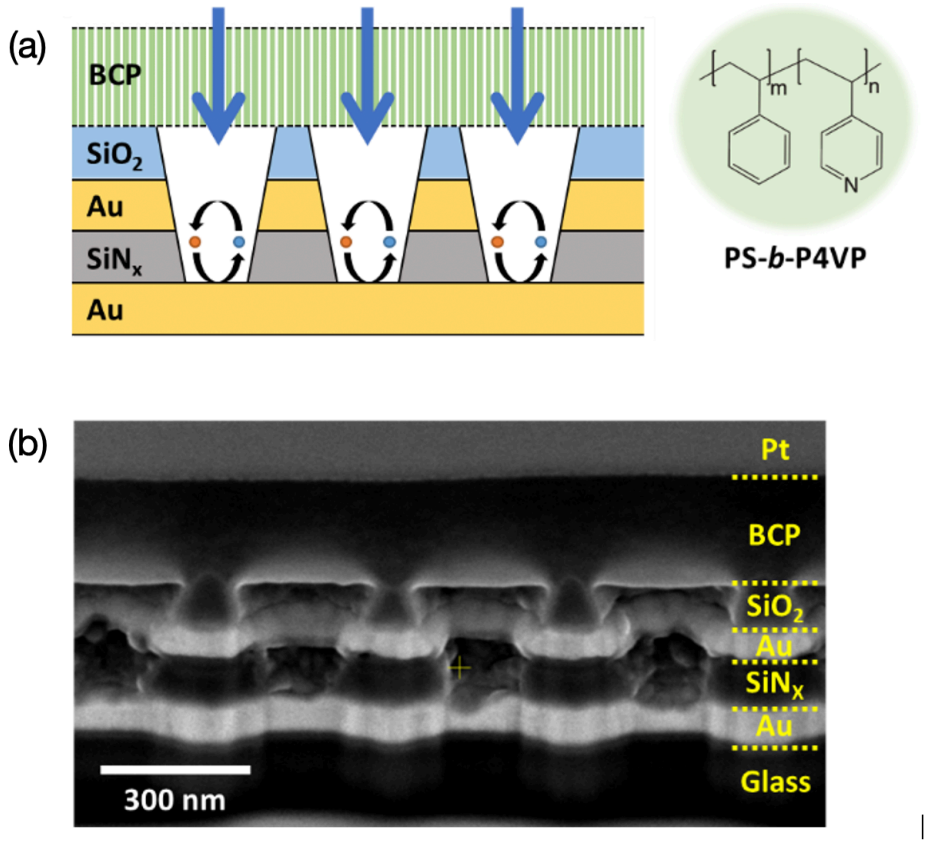

Figure 5. Hierarchically organized multi-component nanostructures employing NEAs. (a) Schematic illustration of a PS-*b*-P4VP BCP@NEA device. (b) Cross-sectional SEM image illustrating the structural integrity of the BCP membrane. Note that the bottom Au layer shown in panels (a) and (b) is left intact to serve as a disk electrode in these redox cycling experiments.

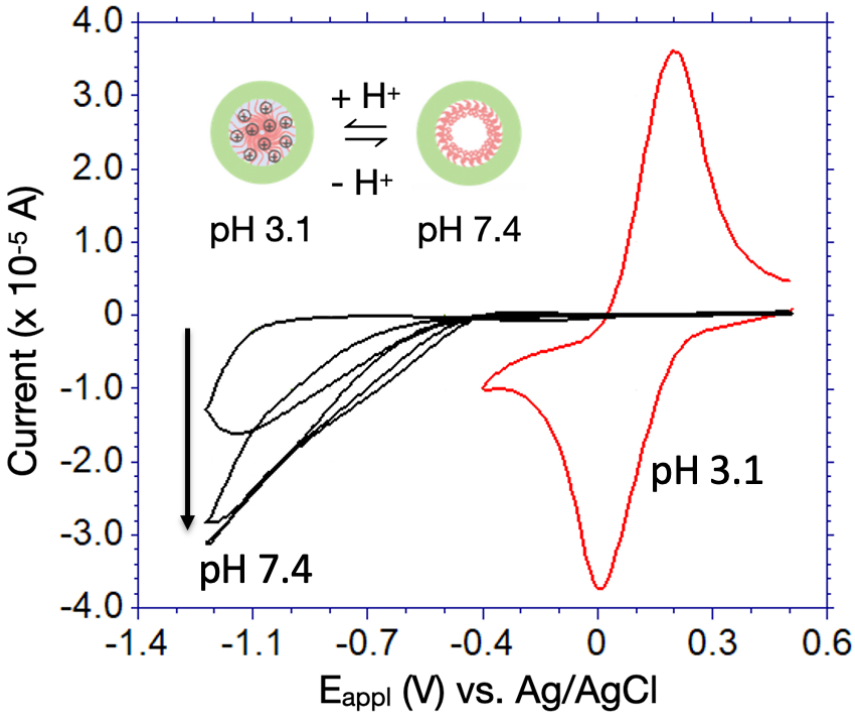

Figure 6. Potential-induced wetting/dewetting phenomena in BCP film controls transport of redox species. Voltammograms of 1 mM $Fe(CN)_6^{3-}$ at pH 7.4 (black) and pH 3.1 (red) on a BCP membrane-coated Au electrode. The black arrow indicates current response with increasing scan numbers (1–3 as shown by the arrow) at pH 7.4. The BCP membrane is prepared by spin-coating PS-*b*-P4VP onto a planar Au electrode at 3000 rpm. The same BCP-coated Au electrode is used in both measurements. *Inset*: Schematic diagram illustrating the structural change responsible for the pH-dependent wetting/dewetting transition.

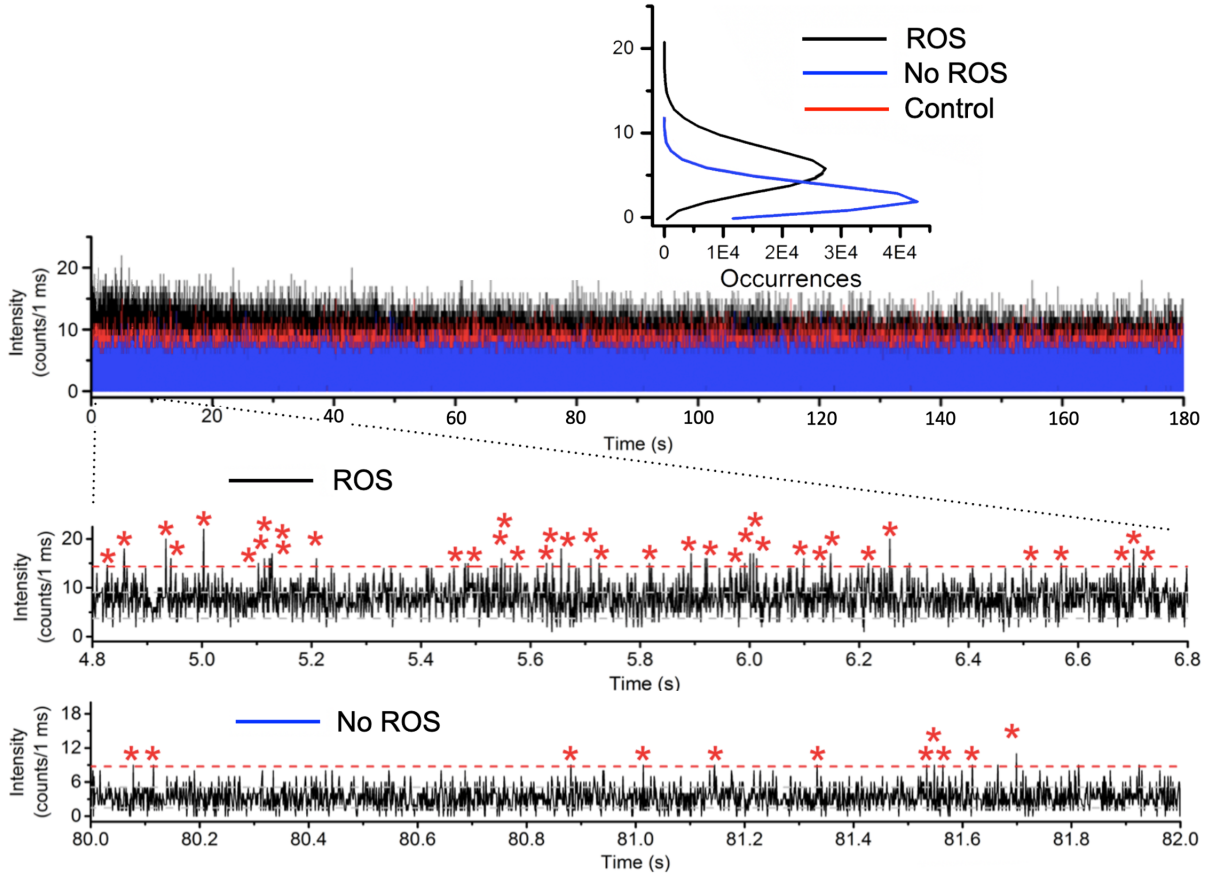

Figure 7. Real-time observation of fluorescence dynamics of single enzyme reactions. (Bottom) E_B (potential of the bottom Au electrode) = -0.6 V, E_t (potential of the top Pt electrode) = open circuit, (Middle) E_B = -0.6 V, E_t = -0.6 V. Asterisks (*) denote events exceeding 3σ for photon emission.

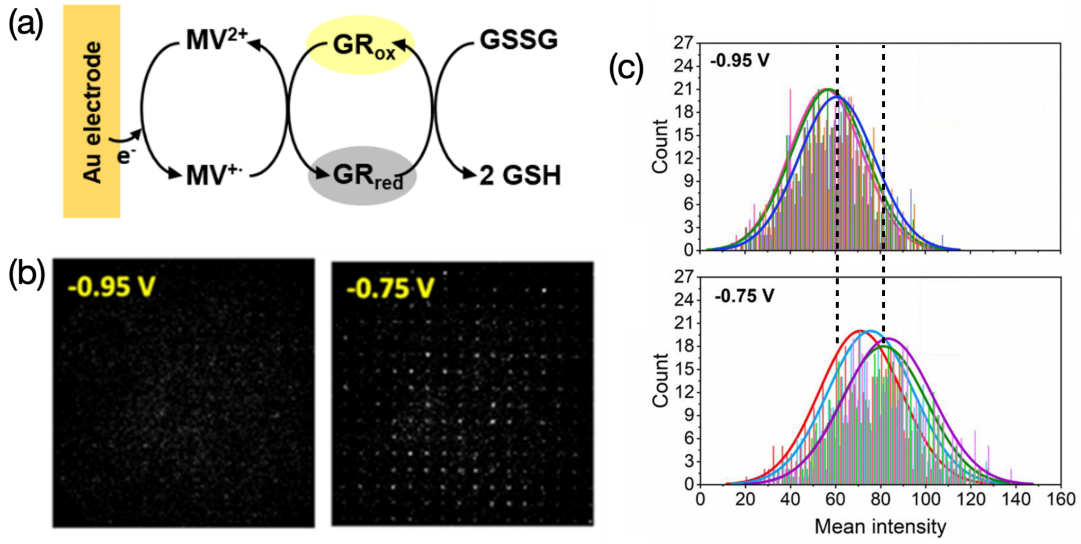

Figure 8. Methyl viologen-mediated single GR molecule potential dependent fluorescence. (a) Cascade reactions supporting sequential electron transfer from Au electrode to MV, GR, and finally GSSG. (b) Fluorescence images of a sub-array containing MV and GR, obtained at reducing (–0.95 V, *left*) and oxidizing (–0.75 V, *right*) potentials. (c) Representative histograms of fluorescence signals from a single pore at each applied potential for GSSG concentrations 0 - 5 mM. Dashed lines indicate the centroid of the Gaussian fit to the 1 mM histograms at each potential.

Supporting Information for

Multifunctional Nanopore Electrode Array Method for Characterizing and Manipulating Single Entities in Attoliter-Volume Enclosures

Seol Baek[1], Allison R. Cutri[1], Donghoon Han[2], Seung-Ryong Kwon[3], Julius Reitemeier[1], Vignesh Sundaresan[4#], and Paul W. Bohn[1,4*]

[1]Department of Chemistry and Biochemistry, University of Notre Dame, Notre Dame, Indiana 46556, USA

[2]Department of Chemistry, The Catholic University of Korea, Bucheon, Gyeonggi-do 14662, South Korea

[3]Department of Chemistry and Research Institute of Natural Science, Gyeongsang National University, Jinju, 52828, South Korea

[4]Department of Chemical and Biomolecular Engineering, University of Notre Dame, Notre Dame, Indiana 46556, USA

[*]Author to whom correspondence should be addressed, *pbohn@nd.edu*.

[#]Current address: Department of Chemistry and Biochemistry, University of Mississippi, University, MS 38677.

Experimental Details

Work described in this paper depends to a considerable degree on access to robust, yet flexible, methods of nanofabrication. The principal design and fabrication approaches used to accomplish the experiments described in the main text are given here.

Construction of High Precision Nanopore Electrode Arrays (*NEAs*). Nanopore electrode arrays used in these studies were fabricated to contain 1-3 metallic layers interspersed with dielectric layers, such as silicon nitride (SiN_x) and silicon dioxide (SiO_2), to form MI, MIMI, and MIMIMI (M = metal, I = insulator) architectures. Typically, the bottom electrode was photolithographically patterned using AZ5214E photoresist and *ca*. 100 nm Au or Pt was deposited on a precleaned glass slide using an electron-beam evaporator. Lift-off was then conducted in acetone to develop the electrode pattern only on the glass slide, while detaching Au deposited in the unwanted areas. Next, a 100 nm SiN_x dielectric layer was deposited by plasma-enhanced chemical vapor deposition (PECVD) to provide electrical insulation between metal layers. Using the same method, 1 or 2 additional metal layers were deposited and patterned on the SiN_x surface. In the final step, a hydrophilic SiO_2 layer was deposited on the top Au layer by PECVD to facilitate nanopore-filling with aqueous solutions and to insulate the top Au electrode from direct contact with the bulk electrolyte solution. An adhesion layer of 5 nm Ti was pre-deposited before each metal or insulator deposition to support structural robustness.

Focused-ion beam (FIB) milling was used exclusively to fabricate high precision nanopore arrays, especially with small pore diameters (d < 300 nm at the top pore surface). FIB milling can generate various nanopore structures simply by adjusting milling parameters, *e.g.*, acceleration voltage, ion current, dwell time, lattice spacing, and array area. In general, ion current is the most important factor determining pore diameter, and in addition to ion current, dwell time and acceleration voltage play a role in determining pore depth. Lattice spacing controls pore density, with smaller spacing corresponding to higher density. As one example, to produce NEAs in a 20 μm × 20 μm square array with a lattice spacing of 250 nm, FIB

operating parameters were set to 30 kV acceleration voltage, 0.28 nA ion current, and 0.1 μs dwell time to produce 350 nm-deep conical frustum-shaped nanopores with top and bottom diameters of 100-120 nm and 60-70, respectively.

Micropore Electrode Arrays. A gold electrode is deposited onto a clean glass slide using electron-beam deposition to serve as the working electrode (WE). While the E-ZMW contains an insulating SiN_x layer, the MEA devices use a 5 μm spacer layer of the photoresist SU-8 2005 to create a substrate deep enough to contain a 3 μm long bacterium. A second, independently-controllable gold electrode is then deposited on top of the spacer layer by e-beam deposition to provide a conductive surface during pore milling. Finally, a 120 nm thick protective layer of SiO_2 is deposited on the top Au layer. Micropores with 1 μm diameter are created in the substrate using FIB milling, as described in the NEA section above, and the device is treated to remove gallium ion buildup from the milling process, as described in the Post-Processing section below. A schematic illustration of an MEA device in cross-section is given in **Figure 3(a)** of the main text.

Massively Parallel Arrays. While direct-writing approaches, like FIB, hold an intrinsic advantage in their precise, nanometer-scale control of NEA structures, these methods are costly, have low throughput, and are time consuming, thus limiting their application to large area motifs and to production of multiple copies. To enable the robust fabrication of massively parallel arrays, we utilize nanosphere lithography (NSL),[1] a technique that incorporates a self-assembled film of nanospheres as a template to create well-ordered arrays of nanopores. It is the favored choice for fabrication when low-cost, high-throughput, and structural control are the principal considerations.[2,3] To begin, a hexagonally close-packed monolayer of polystyrene (PS) latex nanospheres is prepared at an air−liquid interface and then transferred onto the SiO_2 (glass or fused silica, depending on application) substrate by emersing the edge of the device through the bead monolayer at the air-water interface. After transfer, the bead size can be reduced by exposure to an O_2 plasma to control final pore diameter.[4] Then, a thin metal or insulating layer is

deposited onto the nanosphere monolayer, after which the beads are removed to leave an array of circular nanostructures embedded in the deposited layer. While the original pattern of the nanosphere film is ultimately passed on to the photomask, the size of the nanoapertures is determined by the RIE process. Tuning of these experimental parameters enables the fabrication of massively parallel arrays with customized densities.[5]

To obtain NEAs, NSL is combined with reactive ion etching (RIE).[4,6-12] The photomask obtained during NSL spatially confines etching to the exposed substrate. Compared to wet etching, dry etching yields superior structural integrity based on preferentially unidirectional etching perpendicular to the surface, yielding inverse conical frustum shaped nanopores with tunable volumes down to the low attoliter range.[5] The incorporation of one or more metal-insulator layers into a multilamellar substrate further extends the scope of attainable motifs, enabling the fabrication of NEAs containing 1 to 3 annular nanoband electrodes upon application of a layer-selective RIE sequence.[10] In addition, modification of the duration and composition of the RIE sequence enables the fabrication of structures in which the bottom electrode is either a ring or a disk.

Post-fabrication Processing. When nanopore arrays are fabricated by FIB with one or more electrode layers, Au redeposition inevitably occurs on the nanopore inner wall during the milling process, as shown in **Figure S1**. This reduces the functionality of the device, and even with only a moderate amount of redeposition can cause a short-circuit between adjacent metal layers. Wet etching is a simple way to remove the redeposited Au on the nanopore inner surface using a dilute, *e.g.*, 1:10 dilution, Au etchant with DI water. Although wet etching is effective in recovering electric insulation between metal layers, it occasionally produces non-uniform nanopore volumes between pores due to different etch rates, which is attributed to the different diffusion rates of the Au echant into the nanopores and arbitrary redeposition patterns/events on the inner pore wall.

In addition to Au redeposition, gallium ions (Ga^+) can also be implanted into the shallow,

surrounding materials of the nanopores, which may also cause short-circuits.[13] To eliminate the implanted Ga^+, the fabricated NEAs are immersed in a solution of 1M KOH: 1M H_2O_2 for 3 h. Interestingly, after treating the NEAs in this manner, a coil-like thin gold structure was observed in all nanopores, **Figure S2(a)**. Occasionally, no short-circuit is found, indicating the complete detachment of redeposited Au from the pore wall. Otherwise, ~10s treatment with Au etchant (1:10 diluted Au etchant) is enough to remove the redeposited Au on the SiNx to recover an electrically insulating state, **Figure S2(b)**.

Block Copolymer Membrane-Coated NEA Structures. Hierarchically-organized block copolymer (BCP) membrane-coated NEAs, *i.e.*, BCP@NEAs, are constructed by sequential BCP membrane fabrication/processing on Si followed by membrane transfer onto the NEA surface. As an example, pH-responsive polystyrene-*b*-poly(4-vinylpyridine) (PS_{48400}-*b*-$P4VP_{21300}$, M_w/M_n = 1.09) BCP membranes are prepared by spin-coating ~2.5 wt% PS-*b*-P4VP in 1,4-dioxane on cleaned Si wafer surfaces at speeds varying between 500 - 6000 rpm for 1 min. The membrane thickness is tunable from tens of nanometers to a few micrometers by adjusting the spin-coating speed and time and polymer solution concentration. BCP membranes obtained by this process are immersed in selective solvent, *e.g.*, ethanol is selective for P4VP blocks, for 30 min to enable reconstruction and the formation of porous nanocylindrical blocks.

After rinsing with ethanol and blow-drying with nitrogen, BCP membranes are transferred from Si onto the NEA surface by one of two transfer methods: either thermal release tape (TRT) or a water-soluble sacrificial polymer layer. For the TRT-assisted membrane transfer method, a BCP membrane prepared on Si wafer is attached to a single-sided TRT which adheres tightly at room temperature, but losses adhesive strength when heated to 120°C for 30 s. Next, the entire structure, *i.e.*, TRT/BCP/Si, is immersed in water for 10 min to facilitate the Si wafer separating from the TRT-attached BCP membrane in water. After drying, the TRT/BCP is cut to an appropriate size, and the BCP side is attached to an O_2 plasma-cleaned NEA surface. To remove the TRT from the BCP membrane, the TRT/BCP/NEA device is

again heated to 120°C for 1 min, resulting in the final BCP@NEA structure.

In some applications, the TRT membrane transfer process exhibits limited compatibility with heat-sensitive samples. To address these situations, the sacrificial layer approach is used. We begin by coating a thin layer (< 1 μm, *typ.*) of water soluble polyacrylic acid (PAA) onto Si to serve as the sacrificial layer. Subsequently, a PS-*b*-P4VP solution is spin-coated onto the PAA layer and processed as described above to yield a Si/PAA/PS-*b*-P4VP multilayer structure. Upon immersion in aqueous media, *e.g.*, buffer solution for biocompatibility, the PAA layer dissolves, and the BCP membrane detaches and floats to the solution surface. Then, the membrane is transferred and attached to the sample surface mechanically, yielding the desired hierarchically organized BCP@NEA structure in a room temperature process.

Supplemental Figures

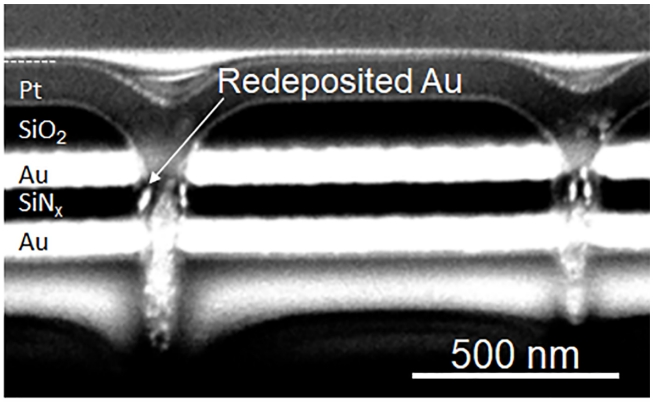

Figure S1. Redeposition during FIB milling. Cross-sectional SEM image of ring-ring 2-electrode nanopores showing redeposited Au layer on the SiN_x dielectric produced during FIB milling. Pt was deposited prior to cross-sectional imaging to improve image quality.

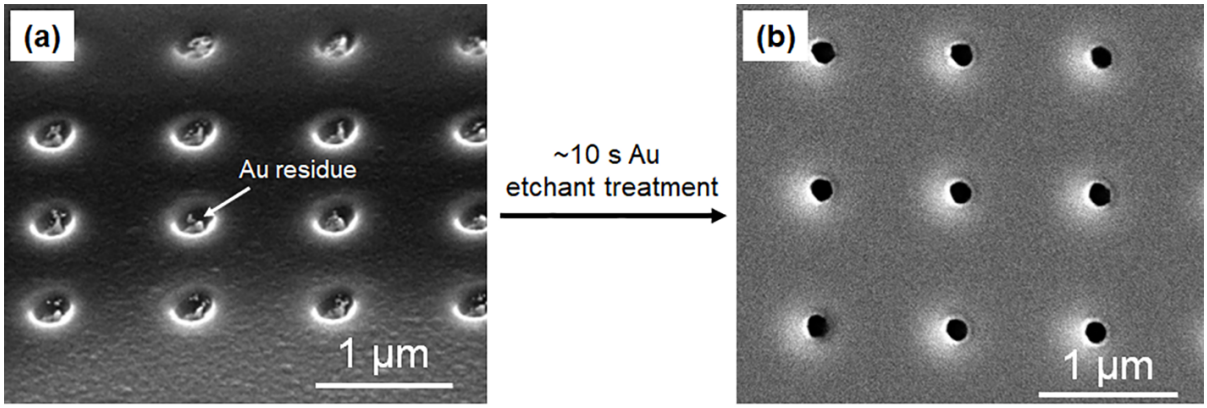

Figure S2. Post-processing to address Au redeposition during Ga ion etching. (a) Tilted (52˚) SEM image after immersing in 1 M KOH: 1M H_2O_2 solution for 3 h. (b) Plan view SEM image after 10 s treatment of the NEA device with Au etchant.

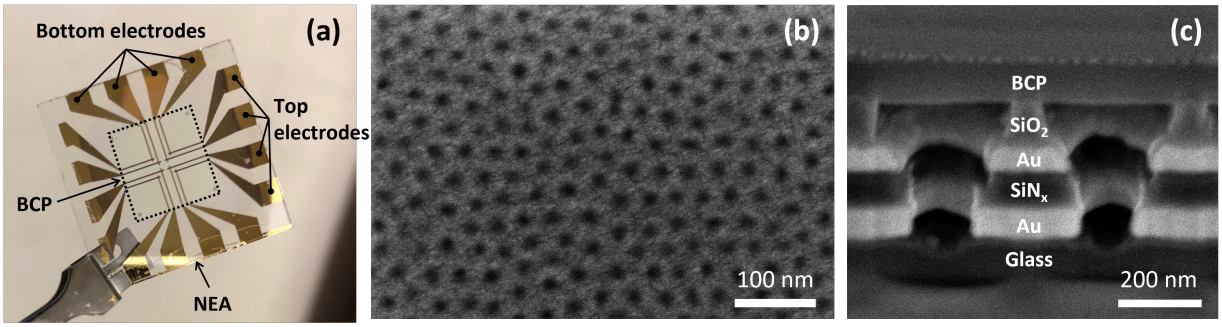

Figure S3. Construction of BCP@NEA structures. (a) Photograph showing eight separate device structures, each consisting of overlapping bottom and top electrodes. (b) Top-view SEM image of a PS-*b*-P4VP BCP membrane. (c) Cross-sectional SEM image of a dual-ring PS-*b*-P4VP BCP@NEA architecture. Composition of individual layers of the MIMI structure are labeled. The BCP layer provides a structurally robust architecture consistent with its use as a pH- and charge-tunable gating layer controlling access to the vestibule of the NEA.

References

[1] U. C. Fischer and H. P. Zingsheim, Journal of Vacuum Science and Technology **19,** 881 (1981).

[2] H. Li and N. Wu, Nanotechnology **19,** 275301 (2008).

[3] J. Hees, R. Hoffmann, A. Kriele, W. Smirnov, H. Obloh, K. Glorer, B. Raynor, R. Driad, N. Yang, and O. A. Williams, ACS Nano **5,** 3339 (2011).

[4] C. Ma, N. M. Contento, L. R. Gibson, and P. W. Bohn, ACS Nano **7,** 5483 (2013).

[5] K. Fu, D. Han, C. Ma, and P. W. Bohn, Faraday Discuss. **193,** 51 (2016).

[6] S. Baek, S.-R. Kwon, K. Fu, and P. W. Bohn, ACS Appl. Mater. Interf. **12,** 55116 (2020).

[7] K. Fu, D. Han, S.-R. Kwon, and P. W. Bohn, ACS Nano **12,** 9177 (2018).

[8] K. Fu, D. Han, C. Ma, and P. W. Bohn, Faraday Disc. **193,** 51 (2016).

[9] K. Fu, D. Han, C. Ma, and P. W. Bohn, Nanoscale **9,** 5164 (2017).

[10] S.-R. Kwon, S. Baek, K. Fu, and P. W. Bohn, Small **20,** 1907249 (2020).

[11] S.-R. Kwon, K. Fu, D. Han, and P. W. Bohn, ACS Nano **12,** 12923 (2018).

[12] C. Ma, N. M. Contento, and P. W. Bohn, J. Am. Chem. Soc. **136,** 7225 (2014).

[13] Z. Han, M. Vehkamäki, M. Mattinen, E. Salmi, K. Mizohata, M. Leskelä, and M. Ritala, Nanotechnology **26,** 265304 (2015).